Landslides induced by the 2017 Mw7.3 Sarpol Zahab earthquake (Iran)

Aya Cheaib, Pascal Lacroix, Swann Zerathe, Denis Jongmans, Najmeh Ajorlou, Marie-Pierre Doin, James Hollingsworth, Chadi Abdallah

Landslides journal

Landslides induced by the 2017 Mw7.3 Sarpol-Zahab earthquake (Iran)

Aya Cheaib[1,2], Pascal Lacroix[1], Swann Zerathe[1], Denis Jongmans[1], Najmeh Ajorlou[3], Marie-Pierre Doin[1], James Hollingsworth[1], and Chadi Abdallah[2]

[1]ISTerre - Université Grenoble Alpes, IRD, CNRS, IFSTTAR, Université Savoie Mont Blanc, CS 40700, 38058 GRENOBLE Cedex 9 Grenoble, France.

[2]Lebanese National Council for Scientific Research/Remote Sensing Center, Blvrd Sport City, Bir Hassan, P.O. Box 11-8281, Beirut, Lebanon.

[3]Department of earth science, Institute for Advanced Studies in Basic Sciences(IASBS), 444 Prof. Yousef Sobouti Blvd., Zanjan 45137-66731, Iran.

Correspondence to: Aya Cheaib (aya.cheaib@univ-grenoble-alpes.fr)

Abstract. Landslides are the main secondary effects of earthquakes in mountainous areas. The spatial distribution of these landslides is controlled by the seismic ground motion and the local slope stability. While gravitational instabilities in arid and semi-arid environments are understudied, we document the landslides triggered by the Sarpol-Zahab earthquake (November 12, 2017, Mw7.3, Iran/Iraq border), the largest event ever recorded in the semi-arid Zagros Mountains. An original earthquake-induced landslide inventory was derived, encompassing landslides of various sizes and velocities (from rapid disrupted rockfalls to slow-moving coherent landslides). This inventory confirms the low level of triggered landslides in semi-arid environments. It also displays clear differences in the spatial and volumetric distributions of earthquake-induced landslides, having a 386 rockfalls of limited size triggered around the epicenter, and 9 giant (areas of ca. 10^6 m^2) active and ancient rockslides coseismically accelerated at locations up to 180 km from the epicenter. This

unusual distant triggering is discussed and interpreted as an interaction between the earthquake source properties and the local geological conditions, emphasizing the key role of seismic ground motion variability at short spatial scales in triggering landslides. Finally, the study documents the kinematics of slow-moving ancient landslides accelerated by earthquakes, and opens up new perspectives for studying landslide triggering over different time-scales.

1 Introduction

Slope failures are one of the main secondary effects of earthquakes (Marano et al., 2010), with a large part of co- and post-seismic damage caused by landslides in mountainous areas (Fan et al., 2019; Keefer, 2002; Marc et al., 2015). The spatial distributions of earthquake-induced landslides highlight trigger parameters related to the earthquake parameters such as the moment magnitude and proximity to the fault (Rodríguez et al. 1999; Keefer 2002), the position in the hanging/footwall of faults (Gorum et al., 2011), or the fault rupture kinematics (Gorum et al., 2014; Specht et al., 2019). Trigger parameters are also related to the site conditions such as the geology (Bozzano et al., 2008; Roback et al., 2018), the groundwater (Watkinson and Hall, 2019), or the topography (Meunier et al., 2008; Lacroix et al., 2013). Complex interactions between these different factors can generate variability in seismic ground motions across a range of spatial scales, which is a key factor influencing landslides spatial distribution in mountainous areas. Subsequent questions arise on the characteristics of the seismic ground motion at the origin of the triggered landslide in relation to the corresponding mechanical behavior of soils and rocks under dynamic loading (e.g. frequency content, amplitudes, duration, Harp and Wilson, 1995; Meunier et al., 2007; Tatard et al., 2010; Harp et al., 2014; Specht et al., 2019; Valagussa et al., 2019). Landslides may also be induced at unexpectedly large distances from the epicenter, in relation to slope susceptibility, site effects, and/or antecedent rain (Delgado et al., 2011). These complexities make it difficult to quantify the controlling factors of earthquake-triggered landslides, which still remains an open question.

In the literature, a recent successful strategy to address this issue has been to compile and analyze all available coseismic landslide inventories (Tanyas et al., 2017; Marc et al., 2016; Tanyas et al., 2019), albeit with a clear under-representation of arid and semi-arid mountainous regions (e.g. Central Andes, Zagros, Tien Shan, Africa, Central Mountain Ranges), even though most of these areas have high seismic activity. This bias can be explained by the low density of population in these regions and the lower level of landslide triggering compared to other tropical or temperate areas for similar earthquake magnitudes (Lacroix et al., 2013, Barlow et al., 2015). Indeed, while shallow disrupted slides in soils and colluvial deposits highly predominate during earthquakes (Harp and Jibson, 1995; Wang et al., 2002; Keefer, 2002) the scarcity of rainfall in arid and semi-arid regions limits weathering and tends to generate hard, thin and dry soils with low organic matter and clay content (Singer., 1991; Dregne, 1976). These properties make soils less sensitive to seismic

shaking, generating fewer shallow disrupted slides in soils and colluvial deposits, which usually predominate during earthquakes in wet conditions (Harp and Jibson, 1995; Wang et al., 2002; Keefer, 2002). Arid and semi-arid regions are, however, of great interest for the study of factors controlling earthquake-triggered landslides, because the interfering effect of rainfall occurs little or not at all and site effects should be limited.

This study analyzes the distribution of landslides triggered by the Sarpol-Zahab earthquake (Mw7.3, Iran) that occurred on November 12th 2017 in the semi-arid (mean precipitation of 230 mm/yr) northwest region of the Zagros Mountains (Fig. 1). This major earthquake, associated with the rupture of a low angle blind thrust fault at depths of 15-20 km (Gombert et al., 2019), occurred at the end of the dry season in an area that encompasses many giant paleo-landslides, of volumes up to 30 km^3 (Ghazipour and Simpson, 2016). Following this earthquake, a few coseismic landslides of various types (debris fall, boulder/rock fall) were reported near the epicenter (Miyajima et al., 2018; Vajedian et al., 2018). The earthquake also reactivated the giant Mela-Kabod landslide (4-km-long, 1-km-wide) located ~40 km south of the epicenter (Vajedian et al., 2018; Goorabi, 2020). To our knowledge, no reactivation was reported at other giant landslides mapped by Ghazipour and Simpson (2016) in the region.

Accordingly, this study, which is based on an exhaustive inventory of the induced landslides, aims at understanding the factors controlling the landslide triggering during this earthquake. Landslide identification relies on a combination of remote sensing techniques, with the objective of detecting landslides of various types and sizes. Following Keefer (1984), we distinguish two main categories: coherent and disrupted slides. A disrupted landslide consists of many semi-independent units or granular flow. Co-seismic disrupted landslides generate scars and/or deposits that are mapped by change detection methods using pre/post- earthquake optical images (Guzzetti et al., 2012). The detection of coherent slow-moving landslides, activated or accelerated by the earthquake, was based on the complementary use of optical image correlation and InSAR time-series analysis.

This study reveals an original distribution pattern of the co-seismic landslides in a semi-arid region, which sheds new light on (1) the earthquake-induced effect on gravitational movements at large distances, (2) the role of seismic amplification, and (3) the co-seismic and post-seismic landslide deformation.

2 Study site

2.1 Geology and landslides of the NW Zagros Mountains

The study area is located in Western Iran, close to the Iraq border, in the local provinces of Kermanshah and Ilam, at the northwest extremity of the Zagros Mountains (Fig. 1a). The Zagros fold and thrust belt (ZFTB) formed in response to the collision between the Arabian and Eurasian plates, which initiated at ~35 Ma (McQuarrie and al., 2003) and continues today with a convergence rate of 8-23 mm/yr (Masson et al., 2014). This ~N-S convergence produced a zone of thin-skinned deformation with a succession of asymmetrical, NW-trending, inverted folds affecting a 7-12 km thick pile of Palaeozoic and Mesozoic to Cenozoic sedimentary rocks, comprising limestone, siltstone, conglomerate, shale and salt (Fig. 1b). For a detailed geological log, the reader can refer to Alavi (2007). The shortening was accommodated along the northwest-trending major thrust faults, which include the Main Recent Fault (MRF; bounding the Zagros to the northeast), the High Zagros Fault (HZF; in the central Zagros), and the Mountain Front Fault (MFF; bounding the belt to the SW) - see Fig. 1b. Regional convergence also implied thick-skin shortening, as most of these faults initiate in the crystalline Arabian basement through the reactivation of older normal faults (Barnhart et al., 2018). The northern part of the ZFTB hosts moderate seismicity (M=5–6) with shallow epicenter depths ranging from 4 to 20 km (Talebian and Jackson 2004; Gombert et al. 2019). The last two significant historical earthquakes in the region (Mw 5.9 and 6.4) occurred a thousand years ago (Ambraseys and Melville 2005). The 2017 Sarpol-Zahab earthquake (Mw 7.3) is the largest event ever recorded in the Zagros mountains.

The topography of the northern ZFTB is strongly controlled by large wavelength folds affecting a succession of stiff calcareous units (Sarvak, Ilam and Asmari Formations), shales (Surgah, Gurpi Formations), or conglomerates (Kashkan Formation), forming ridges and valleys along the anticline and syncline axes, respectively (Alavi, 2007; Homke et al., 2009; Saura et al., 2011). Erosion and fluvial incision have carved this geological structure, revealing the contrast in competence between the stratigraphic units through morphological features such as typical cuesta landforms, breached anticlines, and secondary valleys that developed in less competent units.

This semi-arid zone receives about 230 mm/yr of annual rainfall, which occurs mostly between November and May. Despite the semi-arid conditions, several giant landslides were reported in the ZFTB, including the Seymareh rockslide-rock avalanche that was probably seismically triggered ten thousand years ago (Roberts and Evans 2013). The latter is considered to be the largest terrestrial slope failure (volume 44 km^3) ever known on Earth (Delchiaro et al. 2019). Ghazipour and Simpson (2016) provide a general inventory of large landslides for the ZFTB based on a review of geological mapping, complemented by manual mapping with Google Earth and Digital Elevation Models (DEMs) and

were able to identify about three hundred large paleo landslides with areas ranging between 10^3 m^2 and 10^8 m^2. The landslides reported by Ghazipour and Simpson (2016) and located in our study area are plotted in Fig. 1b. Nonetheless, Ghazipour & simpson didn't give clear explanation for the existence of these slides or showed signs of recent activities.

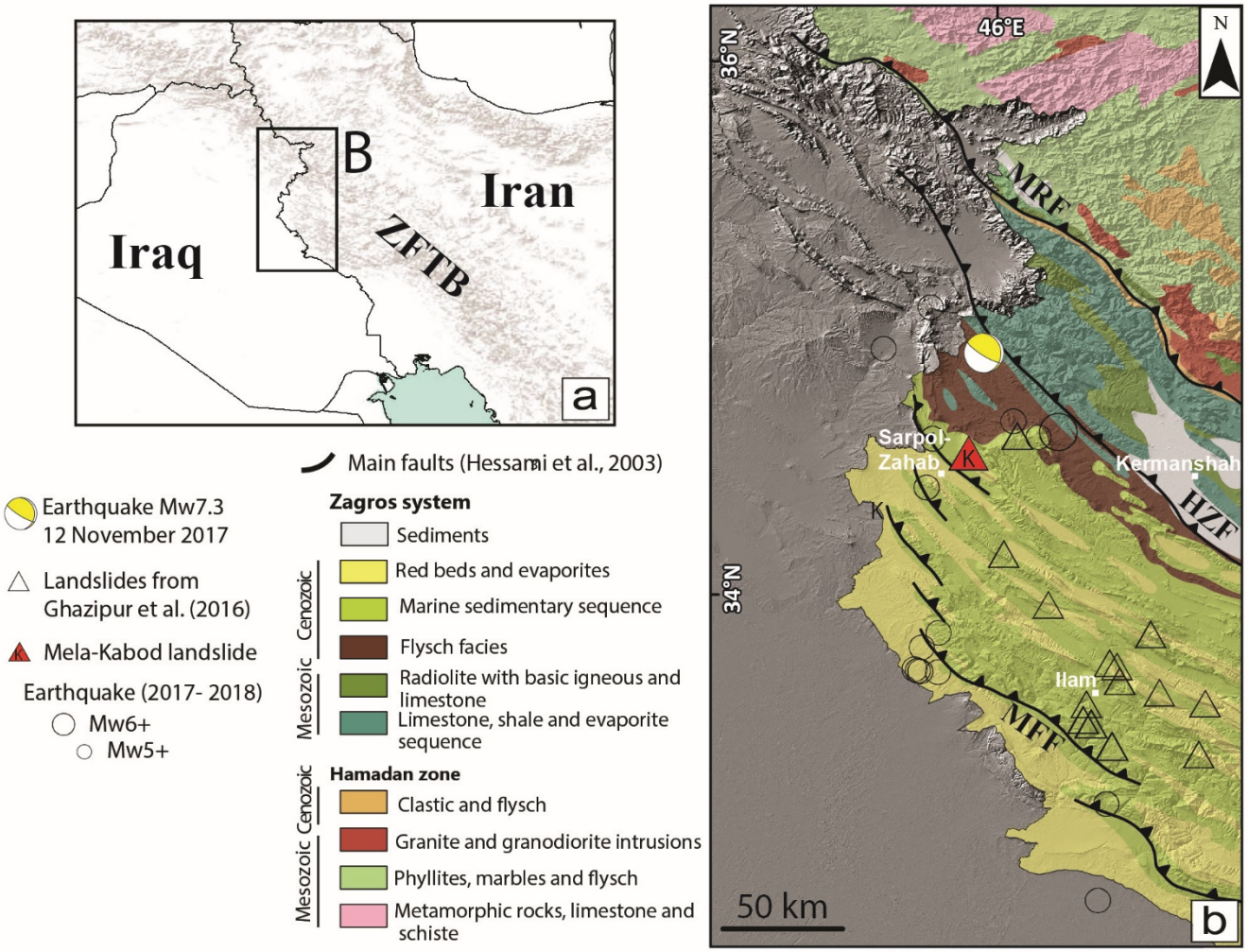

Fig. 1 (a) Study area location. (b) Geological map of the Northwestern Zagros adapted from the 1:2,500,000 tectonic map of the National Iranian Oil Company (Huber, 1976). The yellow beachball is the moment tensor estimated by the US Geological survey (USGS) for the 12 November 2017 earthquake. Earthquakes (Mw>5) are also reported from the USGS for the period of 2017-2018 and presented with empty circles. The empty triangles correspond to the giant landslides mapped by Ghazipur and Simpson (2016) while the red triangle shows the location of the Mela-Kabod landslide (Vajedian et al., 2018; Goorabi, 2020). The main faults are from Hessami et al. (2003). MRF: Main Recent Fault; HZF: High Zagros Fault; MFF: Main Frontal Fault.

2.2 The 2017 Sarpol Zahab earthquake and coseismic induced landslides

The Mw7.3 Sarpol-Zahab earthquake occurred on the 12/11/2017. The EQ epicenter was located at ca. 35°N – 46°E, about 60 km north to Sarpol-Zahab city, close to the lineament of the HZF fault (Fig. 1b). It killed 620 people and caused considerable damage, especially in the city of Sarpol-Zahab (Miyajima et al., 2018). Several recent studies (e.g. Barnhart et al., 2018; Chen et al., 2018; Nissen et al., 2019; Gombert et al., 2019) investigated the earthquake source properties, and fault rupture process, using a combination of radar interferometry (InSAR) and seismology (body waveform inversion), and discussed the tectonic context of this earthquake. These studies reached mainly the following conclusions: (1) the fault rupture did not reach the surface, the earthquake occurred along a blind thrust fault dipping (east) 10-20° and located at a depth of about 14-20 km in the crystalline basement; (2) afterslip may have propagated aseismically up-dip of the earthquake epicenter onto a nearly horizontal basal decollement of the thin-skinned ZFTB; (3) the fault rupture was about 50 km long and 30 km wide with a maximum coseismic slip of 5.5 ± 0.5 m; (4) a high impulsive source with a southward rupture directivity is inferred, and produced the largest peak ground acceleration (PGA = 0.700 cm/s^2) in the city of Sarpol-Zahab (~60 km south of the epicenter); (5) high horizontal peak ground accelerations (~100 cm/s2) were also recorded up to 150 km south of the source (Babaie Mahani and Kazemian, 2018).

Miyajima et al. (2018) reported several coseismic rockfalls and landslides that affected roads and houses around the Sarpol Zahab town, including the triggering of a massive landslide (4×1 km) named Mela-Kabod and located a few kilometers south-east of Sarpol Zahab (Fig. 1b). Coseismic interferometric measurements reveal decorrelation along or close to pre-existing faults, suggesting surface processes (Vajedian et al., 2018) that were not precisely mapped. Authors also estimated that the surface motions at the Mela-Kabod landslide reached over 30 and 10 meters in the horizontal and vertical directions, respectively (Vajedian et al., 2018; Goorabi, 2020). However, to our knowledge, no comprehensive inventory of Sarpol Zahab earthquake-induced landslides has been made, and the possible coseismic effects on the many large paleo landslides identified in this region have not been studied.

3 Data and Methods

The working strategy aimed at detecting the maximum possible number of earthquake-induced landslides in the study area, extending more than 200 kilometers along the Iran-Iraq border using different remote sensing methods (Fig. 2). First, the scars and deposits of disrupted coseismic landslides were mapped by a visual comparison of pre- and post-seismic Planet satellite images. Second, the slow-moving coherent landslides (velocities ranging from m/yr to mm/yr) were

detected by deriving the ground deformation from optical image correlation (Planet and Spot6/7 images) and from radar satellite images (Sentinel-1 Interferometric Synthetic Aperture Radar) for the co-seismic period. Finally, once slow-moving landslide sites were identified and mapped, their kinematics was studied by deriving time-series of landslide displacements over a 20-month period surrounding the Sarpol Zahab earthquake from InSAR data (Table 1).

Data type / satellites (resolution)		**Dates of Acquisition**	
		Pre-earthquake	**Post-earthquake**
Optical	**Planet (3-4 m)**	19-Oct-2017 (N*) 07-Nov-2017 (S*)	13-Nov-2017 (N*) 17-Nov-2017 (S*)
	SPOT6/7 (1.5 m)	13-Oct-2013 (N*), 24-Apr-2014 (N*), 04-May-2014 (N*), 14-Aug-2014 (N*), 09-Nov-2014 (S*)	29-Nov-2017 (N*), 12-Dec-2017 (N*)
Radar	**Sentinel-1 (~4x15 m)**	10-Jan-2017 to 06-Nov-2017 (acquisition every 12 days)	12-Nov-2017 to 27-Aug-2018 (acquisition every 6 days)

Table.1 Synthesis of satellite data used in this study and their characteristics. N* and S* correspond respectively to the areas around the epicenter and in the Southern part.

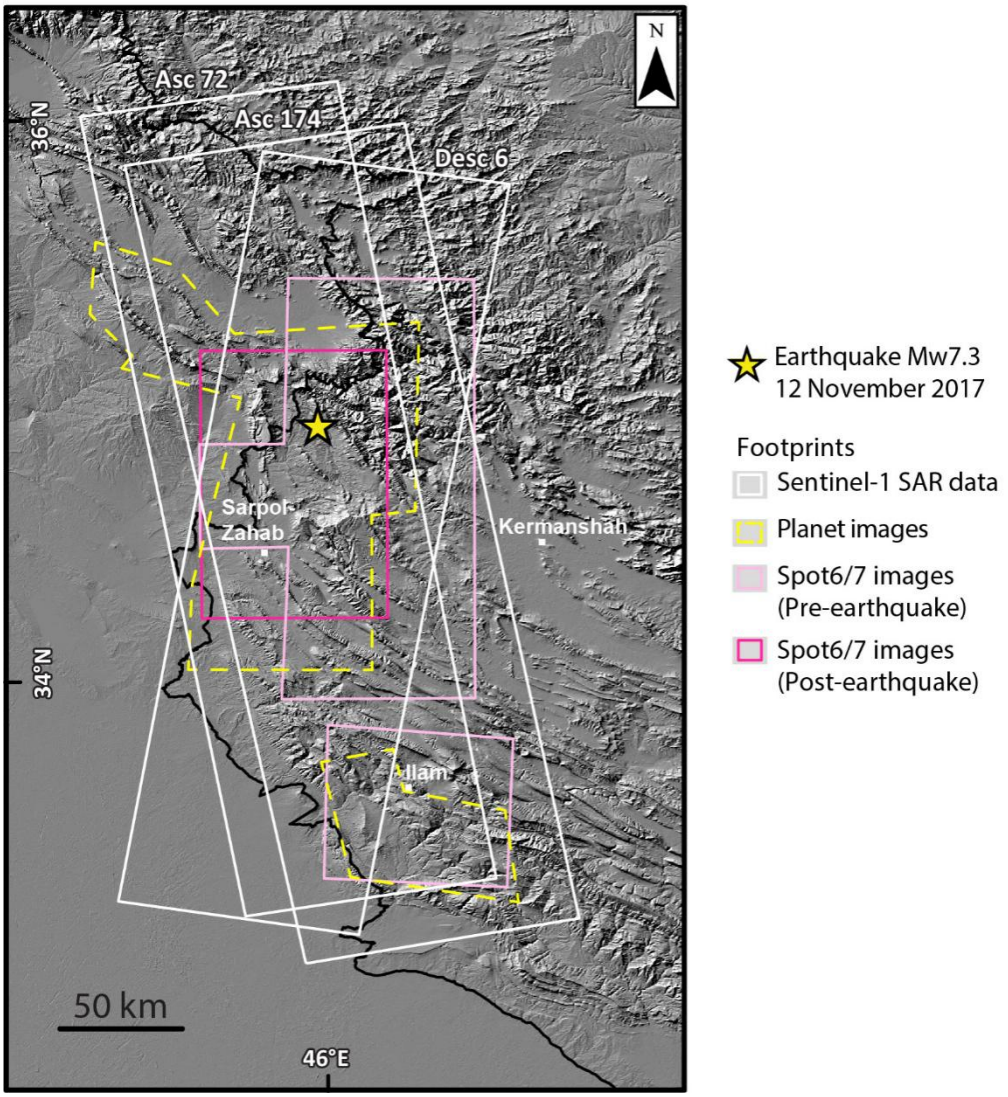

Fig. 2 Footprints of the satellite data used in this study. See Table 1 for the data characteristics.

3.1 Inventory of disrupted landslides

A detailed inventory of coseismic disrupted landslides was conducted by the visual comparison of multispectral Planet satellite images (3-4 m resolution) acquired before and after the earthquake (19/10/2017 and 13/11/2017) covering an area of 12000 km² centered on the epicenter (see footprint on Fig. 2). The available pre- and post-earthquake orthorectified Planet images were compared and analyzed in ArcGIS software using available toolsets, DEMs, and Earth view base maps. The analysis was complemented by geological maps of unequal resolution: the 1:250,000 Ilam province geological map from Llewellyn (1974) and the 1: 2,500,000 Iran tectonic map from the National Iranian Oil Company (Huber, 1976). As shown, for instance, on Fig. 3, we typically detected and mapped new rockfall scars and their associated debris deposits

induced by the earthquake as polygons. To extract the slope of each detected disrupted landslide, a slope map was derived from the high-resolution post-earthquake DEM using arcmap slope (3D analysis) tool (see section 3.2.1). We ascribed to each landslide the steepest slope found within a buffer zone of 50 m around the highest altitude point (i.e. headscarp) of each mapped polygon.

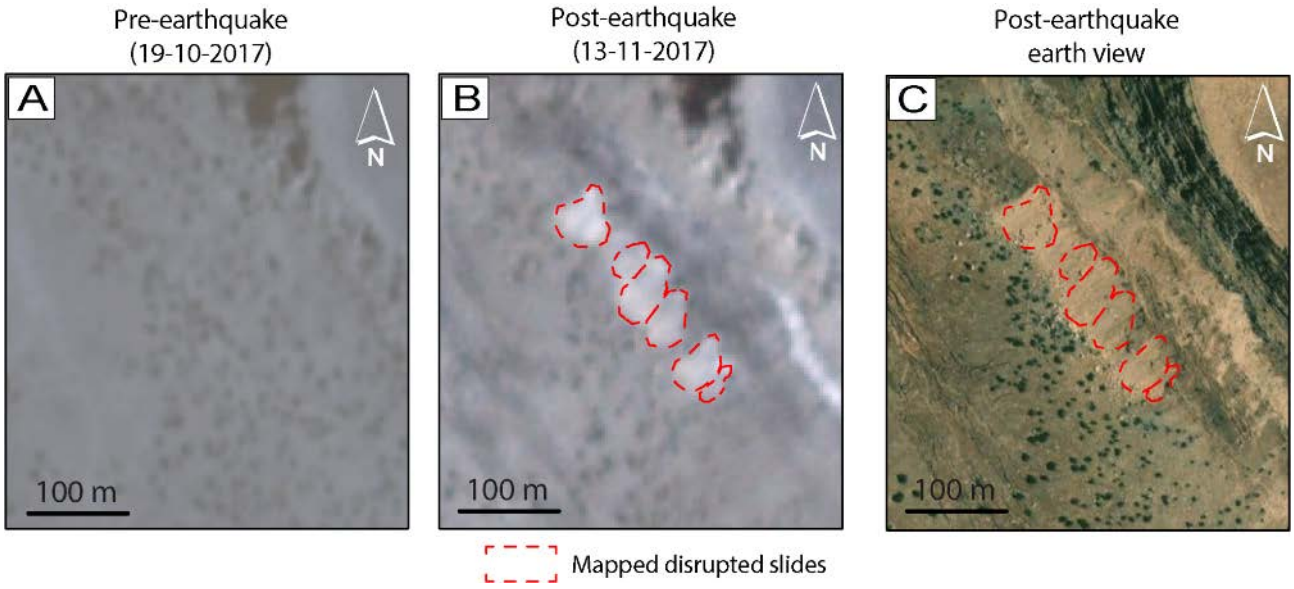

Fig. 3 Typical example of coseismic disrupted landslide deposits mapped from Planet imagery. (a) pre and (b) post Sarpol-Zahab earthquake Planet imagery showing the same area. (c) Post-earthquake Google Earth view.

3.2 Inventory of coherent slow-moving landslides

3.2.1 High resolution DEMs

Two 4 m resolution pre- and post-earthquake DEMs were generated in the region of the epicenter (Fig. 2) from tri-stereo pairs of SPOT6/7 images, acquired in 2014 and November-December 2017 (Table 1). Ames Stereo Pipeline (Beyer et al., 2018) was used for the DEM generation, following the iterative method proposed by Lacroix (2016). A 4 m resolution pre-earthquake DEM was similarly generated with Ames Stereo Pipeline using tri-stereo SPOT7 images (acquired in 2014, Table 1) covering the southern part of the study area (Fig. 2). These DEMs were used both for geomorphological purposes and for precise orthorectification of optical images (see following section).

3.2.2 Correlation of optical images

The earthquake-induced horizontal ground displacement was calculated from the correlation of pre/post-earthquake orthorectified optical satellite images (Leprince et al., 2007), using SPOT6/7 images for the northern area, and Planet satellite images for the southern area where immediate post-earthquake SPOT6/7 images were not available (Table 1). The pre- and post-earthquake panchromatic bands of the SPOT6/7 images from the northern area (Fig. 2) were first orthorectified using the high resolution concurrent DEMs and then mosaicked. The COSI-Corr phase correlator was then used to measure the horizontal ground motion (Leprince et al., 2007). The correlation was conducted in the frequency domain using a sliding window of 64×64 pixels, which was chosen after several trials to maximize the signal to noise ratio on the Mela-Kabod landslide. In a similar manner, the Planet images were correlated (Fig. 2). For that, the green bands were utilized for correlation due to artifacts observed in the other bands.

The EW and NS displacement fields were post-processed to correct them from classical artifacts (e.g. Leprince, et al., 2007; Bontemps et al., 2018): a 2D linear ramp was removed from the data to detrend them and pixels of low correlation coefficient (CC<0.65 for SPOT6/7 and CC<0.7 for Planet images) were masked. Finally, to eliminate a potential constant bias of georeferencing, the median of the displacement in each direction was removed from the entire EW and NS displacement fields (e.g. Lacroix et al. 2018).

These displacement fields were then inspected visually to detect landslide-like patterns of displacement with magnitudes larger than the uncertainty of the displacement (calculated as the standard deviation of the EW and NS components over the whole area), oriented in the direction of the slope. The detected patterns are then plotted on the google-earth image to validate the landslide origin of this signal.

3.2.3 InSAR processing

InSAR data were used to detect and monitor slow coherent landslides. We derived ground motion time-series from InSAR using three Sentinel-1 SAR tracks spanning a 20-month time period centered on the earthquake (Table 1) with acquisitions of 12 and 6 days before and after the earthquake respectively. differential interferograms were generated using the NSBAS (New Small BAseline Subset) (Doin et al., 2011) processing chain based on the ROI_PAC software (Rosen et al., 2004). Two ascending (tracks 174 and 72, subswath iw1 for both) and one descending (track 6, subswath iw2) tracks of Sentinel 1A and 1B covering an area of 33500 km2 (see footprint on Fig. 2 and Table 1) were used for this purpose. Initially, all secondary SLC (Single Look Complex) images in a single reference SLC geometry were resampled and co-registered to

reference using precise orbits and an ASTER digital elevation model (30 m resolution), combined with empirical offsets between secondary and reference images. Then, a small baseline subset was defined using temporal and perpendicular baseline constraints (Doin, et al., 2011). After calculating differential interferograms we corrected them from atmospheric delays using ERA-5 ECMWF (European Center for Median-Range Weather Forecast) reanalysis (Doin et al., 2009). Finally, we made an empirical correction for topographically-correlated atmospheric-delays (Doin et al., 2011).

The coseismic interferograms were then inspected for landslide-like patterns characterized by InSAR fringes with sharp limits delineating spatially small anomalies located on slopes (e.g. Dini et al., 2019). Special attention was paid to the giant paleo-slides identified by Ghazipour and Simpson (2016) to detect potential signs of activity. When a landslide-like pattern is detected, we then inspected the Google Earth images and the generated DEMs to check for typical geomorphological signs of gravitational deformation (i.e. scarps, depletion zones, debris deposits, slope bulging, river deflection, etc.).

The displacement time-series were then retrieved for the detected landslide sites. As the coseismic signals on landslides were too large to be unwrapped, due to phase ambiguities across landslide boundaries, the pre- and post-earthquake time-series were analyzed independently to determine the pre- and post- seismic landslide kinematics. After dividing the interferograms into pre- and post-earthquake groups, phase delays of the unwrapped interferograms were inverted pixel by pixel in order to solve the total phase delay, relative to the first date (Doin et al., 2011). Time-series for each landslide were then constructed using the cumulative deformation maps obtained from the inversion (one map at each date of the Sentinel-1 images). The mean displacement (μ) was calculated over a selected window, of about 15x15 pixels on the landslide body at each date, relative to a mean displacement extracted from a surrounding buffer zone of several hundreds of meter width. The displacement deviation (σ) was then estimated from the mean absolute deviation of the displacement in the reference area.

In a next step, the pre- and post-seismic landslide mean velocities and their associated uncertainties was calculated. Each point "*i*" of the time-series was considered as a random variable of normal distribution (μ_i, σ_i). 10,000 realizations of this random variable were randomly picked at each point of the time series, and the associated 10,000 pre and post velocities were calculated by a linear regression of these time-series. The mean and standard deviation of these 10,000 velocities gave us an estimate of the mean velocity and its uncertainty.

4. Results

4.1 Disrupted landslides

386 coseismic disrupted landslides were mapped (Fig. 4) with areas ranging from 200 to 20000 m^2. These events are spread over 140 km along the fault in the mountain ranges, with the more distant one located 90 km south of the epicenter. They are mostly rockfalls that affect mainly limestone and flysch formations. Approximately 85% of these landslides are located within 40 km of the epicenter, with the highest concentration northwest of the epicenter (Fig. 4). This clustering does not correspond to the coseismic slip of the fault that occurred preferentially southward from the epicenter (Fig. 4). As the fault is blind with a low dip angle, the majority of the disrupted landslides are located some distance to the fault, ranging from 14 to 30 km. As seen in Fig. 4 and Fig. 5, landslide locations present a clear relationship with the topography, with most landslides occurring on slopes between 40° and 80°, which are significantly steeper than the mean ~18° slope of the area (Fig. 5).

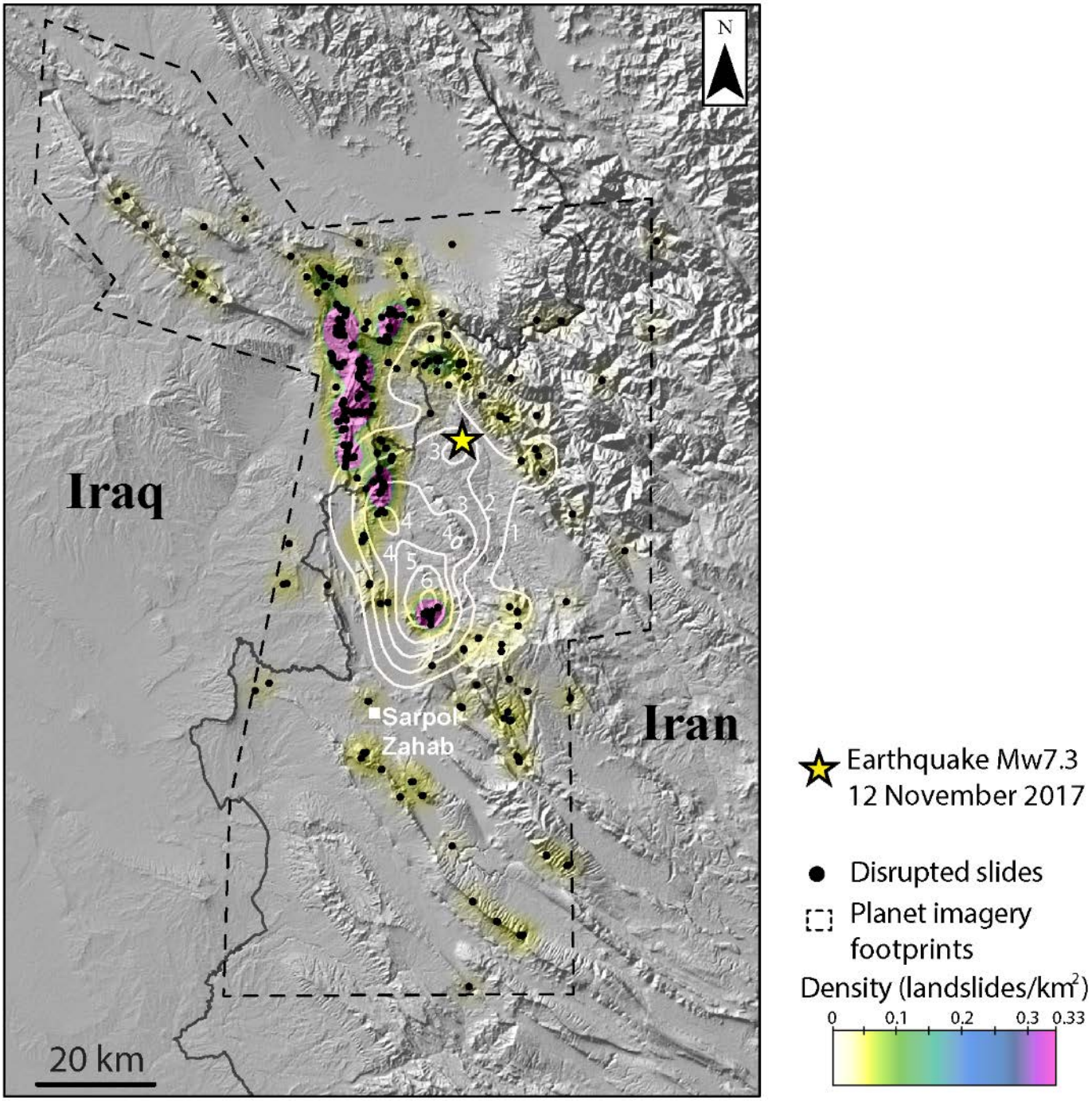

Fig. 4 Disrupted slides and falls inventory, and corresponding density map. White isolines indicate cumulative fault-slip (in meters) 12 seconds after earthquake reported from Gombert et al. (2019).

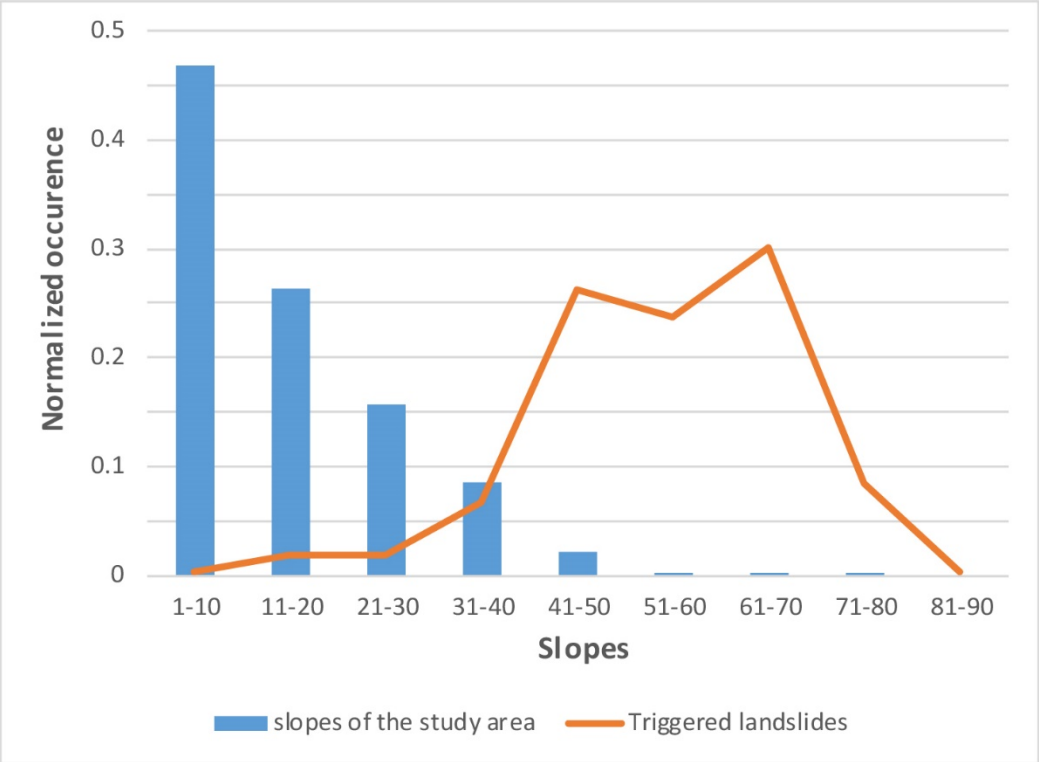

Fig. 5 Normalized number of landslides per slope category, and comparison with the slope distribution in the area of study.

4.2 Coherent landslides

4.2.1 Detection and characterization

Nine coseismically coherent landslides were detected, their locations and properties are summarized in Table 2.

One site located ~40 km south of the epicenter was detected by optical image correlation: the Mela-Kabod landslide (Fig. 6), already reported by Miyajima et al. (2018) and Vajedian et al. (2018). This massive landslide (area 4.5 km^2) affects the red conglomerates of the Kashkan formation underlying the stiff limestone of the Asmari Formation (Valkaniotis et al., 2018). It showed southwestward movement with a maximum horizontal coseismic displacement of about 30 m, in agreement with the value found by Vajedian et al. (2018) using SAR interferometry. The detection threshold was found to be 0.5-1.6 and 1.5-2.2 for SPOT6/7 and Planet image correlation respectively. With this detection threshold, no other earthquake-induced landslides were found in the targeted area.

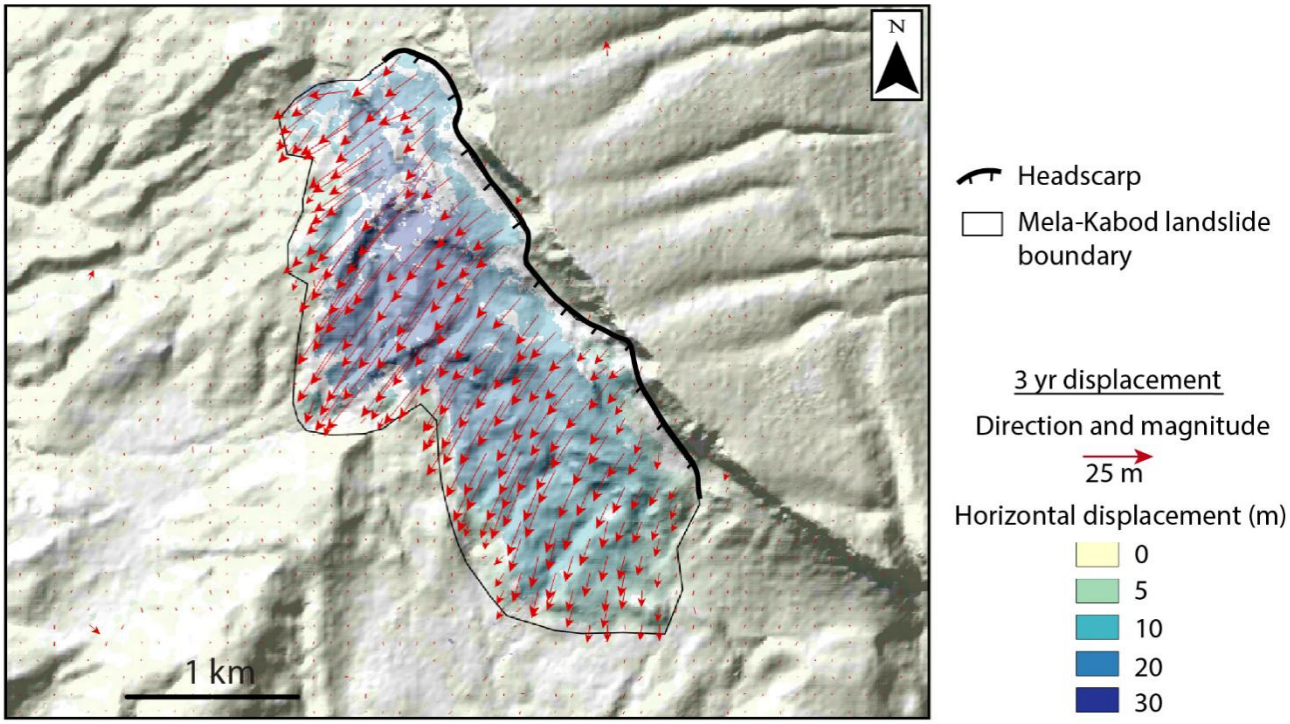

Fig. 6 Spot6/7 image (Table S1) correlation results for the Mela-Kabod landslide obtained using the COSI-Corr tool, showing the 3 yr cumulated displacement in meters including the coseismic period of the Sarpol-Zahab earthquake. The black contour shows the limit of the horizontal displacement field while the displacement direction and magnitude are presented by the red arrows.

Analyzing the coseismic SAR interferogram over the study area (Fig. 7a), eight landslides characterized by sharp phase discontinuities and 3-4 fringes were detected (Fig. 7b and Fig. 7c; Table 2). One landslide; the Bezmir-Abad with an area of 15 km^2 (Fig. 7b) is located 36 km south of the epicenter, close to the Mela Kabod landslide, and also affects the Kashkan and Asmari formations. The other seven landslides are clustered between 140-180 km south of the epicenter (Fig. 7c, Table 2), in a region where no disrupted landslides were detected with the Planet satellite imagery. The size of the affected areas varies between 2 and 7.8 km^2 (see Table 2). Four of these sites (Mehr, Marbera-1, Marbera-3 and Bezmir-Abad) coincide with the location of paleo landslides reported by Ghazipour and Simpson (2016), two are pointed on the geological map (Marbera-1 and Delgosha; see Fig. S1 in supplementary information), while the other two (Sarney-1 and Sarney-2) were previously unknown.

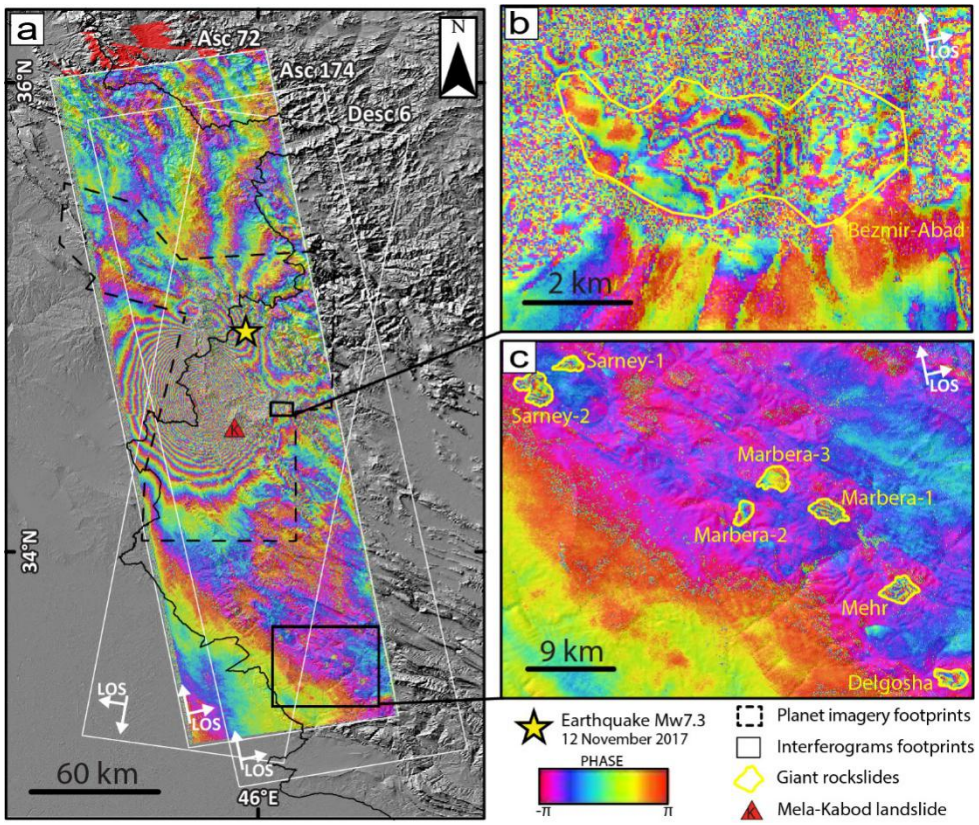

Fig. 7 (a) Coseismic SAR interferogram computed over the study area from the ascending track 72 between 11/11/2017 and 17/11/2017. (b) and (c) close-ups show the 8 landslides detected with InSAR near the earthquake and in the southern far-field, respectively. The location of the Mela-Kabod landslide, detected with optical images, is identified with a red triangle.

Assessment of the geomorphology and the geology of each site revealed clear evidence for pre-existing gravitational slope deformations such as (1) headscarps of pluri decametric height bounding the top of the zones (Table2), (2) slope bulging and river deflection in some cases, and (3) screes and old landslide deposits.

As an example, the geomorphological analysis of the Mehr landslide, located 170 km south of the epicenter, is shown in Fig. 8. The coseismic displacement extent, clearly visible in the interferogram (Fig. 8a), delineates a 3 km long by 2.5 km wide region. It is bounded to the SW by a ~160 m high headscarp and to the NE by the toe of debris deposits that propagate ~600 m over the valley floor (see DEM in Fig. 8b). The geological map (Fig. 8c) and the cross-section (Fig. 8d) indicate that the landslide initiated at the contact between Ilam limestones and Surgah shales, along the northern flank of a NW-SE-striking anticline. The mechanism is a rockslide consisting of stiff limestone blocks sliding over a large distance on a shale layer dipping 5 to 15° NE, and probably eroding it throughout the movement. From Google Earth images, the mass

in motion is destructured with a mixing of limestone blocks, entrained clayey material, and debris deposits probably generated by secondary rockfalls. Comparison between a topographic profile extracted along the rockslide and one taken along the non-disrupted slope suggests a maximum depth of 200 m for the slip surface (Fig. 8d), implying a rockslide volume of ~0.5 km^3.

We found similar geomorphological and geological characteristics for the other sites (Fig. S1 and Table 2) that can be summarized as follows: (1) the detected interferometric patterns match the positions of pre-existing giant rockslides with a volume range from 0.16 to 2.2 km^3, as estimated from the empirical surface/volume law from Ghazipur and Simpson (2016); (2) all rockslides occurred in a geological structure with a limestone layer (Ilam or Asmari formations) overlying a softer rock (shale, marl or conglomerate of the Surgah, Pabdeh and Kashkan formations, respectively); (3) for the seven sites located furthest from the epicenter, the rockslides developed on the flanks of anticlines; (4) as revealed by the headscarp height and the debris propagation, most rockslides exhibit a total displacement of several hundred meters.

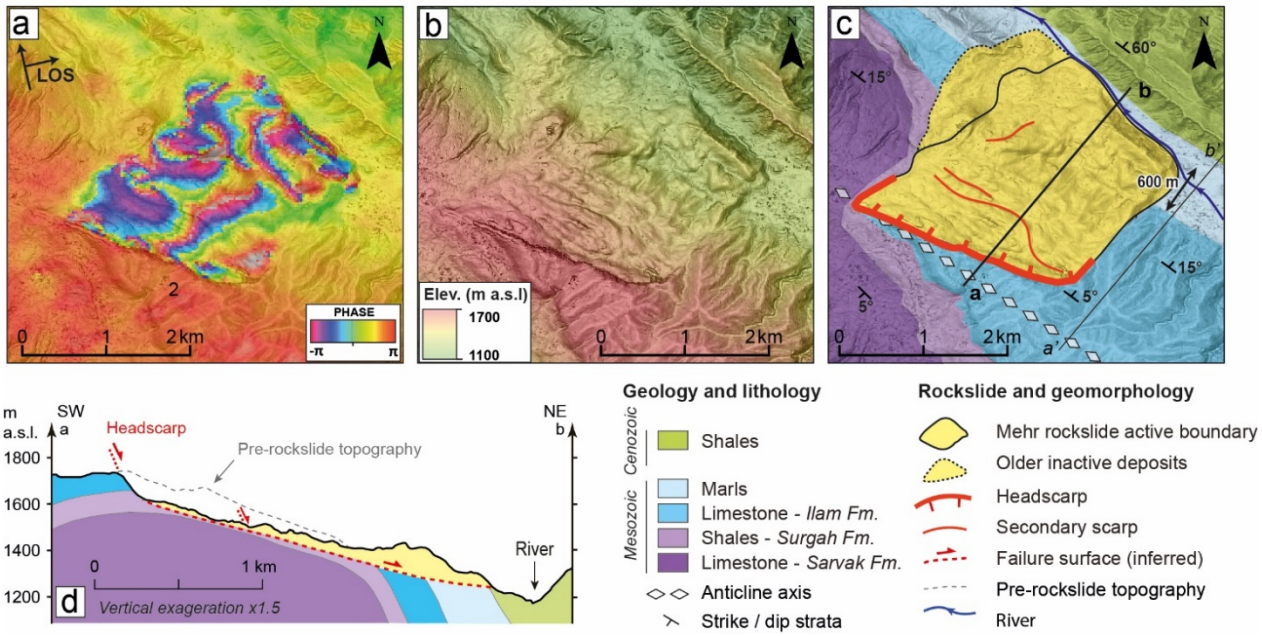

Fig. 8 The Mehr giant rockslide (see location in Fig. 7c) presented from (a) a coseismic interferogram computed along the Sentinel-1 ascending track-72 between 11/11/2017 and 17/11/2017, (b) a pre-seismic SPOT6-7 hillshaded DEM (4 m resolution, 09/09/2014), (c) a geological map adapted from Llewellyn (1974), (d) a cross-section built along the profile "ab" (see location on Fig. 8c). The pre-rockslide topography is presented from the reference profile a'b'.

4.2.2 Co-seismic motion

The precise quantification of the coseismic motion with InSAR data is not possible due to (1) the sharp limits of the patterns in the coseismic interferograms (Fig. 7), which prevent extraction of the phase value during the unwrapping process, and (2) the absence of a displacement signal in the correlation of optical images (Fig. S1). Accordingly, the upper and lower limits of the coseismic motion was bracket using the optical image correlation uncertainty and fringes numbers of the interferogram respectively. The LOS coseismic displacement at the 8 sites previously affected by rock avalanches was estimated to be between a few centimeters and a few tens of centimeters (Table 2).

Landslide name		**Mehr**	**Marbera-1**	**Marbera-2**	**Marbera-3**	**Sarney-1**	**Sarney2**	**Delgosha**	**Bezmir-Abad**	**Mela-Kabod**
Location (°°.dd)	**Longitude**	46.43909	46.36963	46.28953	46.32007	46.12247	46.0821	46.49005	46.10286	45.906
	Latitude	33.4379	33.5133	33.5103	33.5446	33.6532	33.6291	33.3525	34.6157	34.535
Ghazipur and Simpson (2016)	**Name**	L21	L22	NR	L23	NR	NR	NR	L56	NR
	Area (m^2)	$5.2x10^6$	$3.9x10^6$	NR	$6.3x10^5$	NR	NR	NR	$1.6x10^6$	NR
Area (m^2)		$5.8x10^6$	$5.2x10^6$	$2.7x10^6$	$4.9x10^6$	$2.6x10^6$	$7.8x10^6$	$4.4x10^6$	$15x10^6$	$4.5x10^6$
Width (m)		2500	3100	1000	2400	1600	3600	2000	6100	3800
Length (m)		3100	2000	1800	2300	2500	2500	2100	2500	1700
Volume (m^3)		$5.2x10^8$	$4.5x10^8$	$1.7x10^8$	$4.1x10^8$	$1.6x10^8$	$7.8x10^8$	$3.4x10^8$	$2.2x10^9$	$3.5x10^8$
ΔH (m)		410	425	340	550	370	520	520	510	560
Maximum height of headscarp (m)		160	130	30	120	100	160	100	300	> 30
Slope average (◦)		9	10	8	12	9	8	8	10	14
Landslide orientation		North-East	North-East	South-West	North-Northeast	North-East	South-West	South-West	North-East	South-West
Distance from epicenter (km)		169.7	159.7	158.8	155.5	140.1	142.4	179.6	35.8	41.9
LOS velocity (mm/yr)	**Pre-earthquake period**	25.4 ± 3.4	11.8 ± 3.9	0.3 ± 2.3	24.5 ± 4.2	2.6 ± 2.9	2.5 ± 2.3	23.2 ± 6.6	14.6 ± 12.5	0.2 ± 2.0
	Post-earthquake rain period	25.9 ± 8.5	38.1 ± 7.9	6.2 ± 5.6	46.5 ± 7.8	5.9 ± 6.1	9.5 ± 4.5	28.9 ± 6.7	9.1 ± 12.5	13.7 ± 2.0
	Post-earthquake dry period	16.7 ± 16.7	14.8 ± 17.4	2.6 ± 11.7	2.9 ± 16.2	2.5 ± 13.6	10.6 ± 10.6	34.3 ± 11.2	18.1 ± 32.1	28.9 ± 6.7
Range of coseismic displacement (cm)		9 to 40	11.4 to 36	5 to 42	2.9 to 42	5.7 to 75	8.6 to 75	5.7 to 67	11.4 to 50	100 to 3500

Table 2: Characteristics of the giant slow-moving rockslides detected from Sentinel-1 interferograms and optical image correlation. The area of the rockslides already identified by Ghazipur and Simpson (2016) is given for comparison. NR stands for landslides that were Not Reported in the database of Ghazipur and Simpson (2016). The area deduced from this study corresponds to the area affected by co-seismic displacement as seen in the interferograms. The volume is estimated from the empirical law proposed in the study of Ghazipur and Simpson (2016) for the Zagros region. The elevation difference ΔH, average slope and length are calculated from the headscarp top to the landslide toe. Landslide orientation gives the direction toward which the material moves. Line-of-sight (LOS) velocities are calculated by linear interpolation of cumulative displacements from time series over several months (see §3.2.3 for details).

4.2.3 Pre- and post-seismic time-series

The cumulative LOS displacement time-series show different kinematic patterns for the coherent landslides before and after the earthquake (Fig. 9). In the pre-seismic period, landslide velocities range between 0 to 25 mm/yr, with either dormant (almost zero velocity within the error limits: Fig. 9c, d, e, h) or slightly active landslides of constant velocities (Fig. 9b, f, g, i, j). After the coseismic motion, we observe a transient relaxation over 20 days of about 2-5 mm clearly seen at several sites: Mela-Kabod, Marbera-3, Marbera-1 and Mehr (Fig. 9c, f, g, i). Then, three different post-seismic patterns emerge with landslides showing: (1) a constant post-seismic velocity indistinguishable, within uncertainties, of the pre-seismic one (Fig. 9b, d, h, i), (2) a constant post-seismic velocity higher than the pre-seismic one (Fig. 9e, j), and (3) a transient increase in velocity of several months before returning to their pre-seismic rates (Fig. 9c, f, g). In this latter case, the transient increase and its subsequent lower velocity phase coincide with rainy and dry seasons, respectively, as shown by the comparison with rainfall time-series (Fig. 9a). Finally, the displacement observed for the last acquisition date of the Bezmir Abad time series (Fig. 9b) may correspond to the coseismic effect of a Mw 6.0 earthquake that occurred in the vicinity (~13 km) of this site (Fig. S4).

347

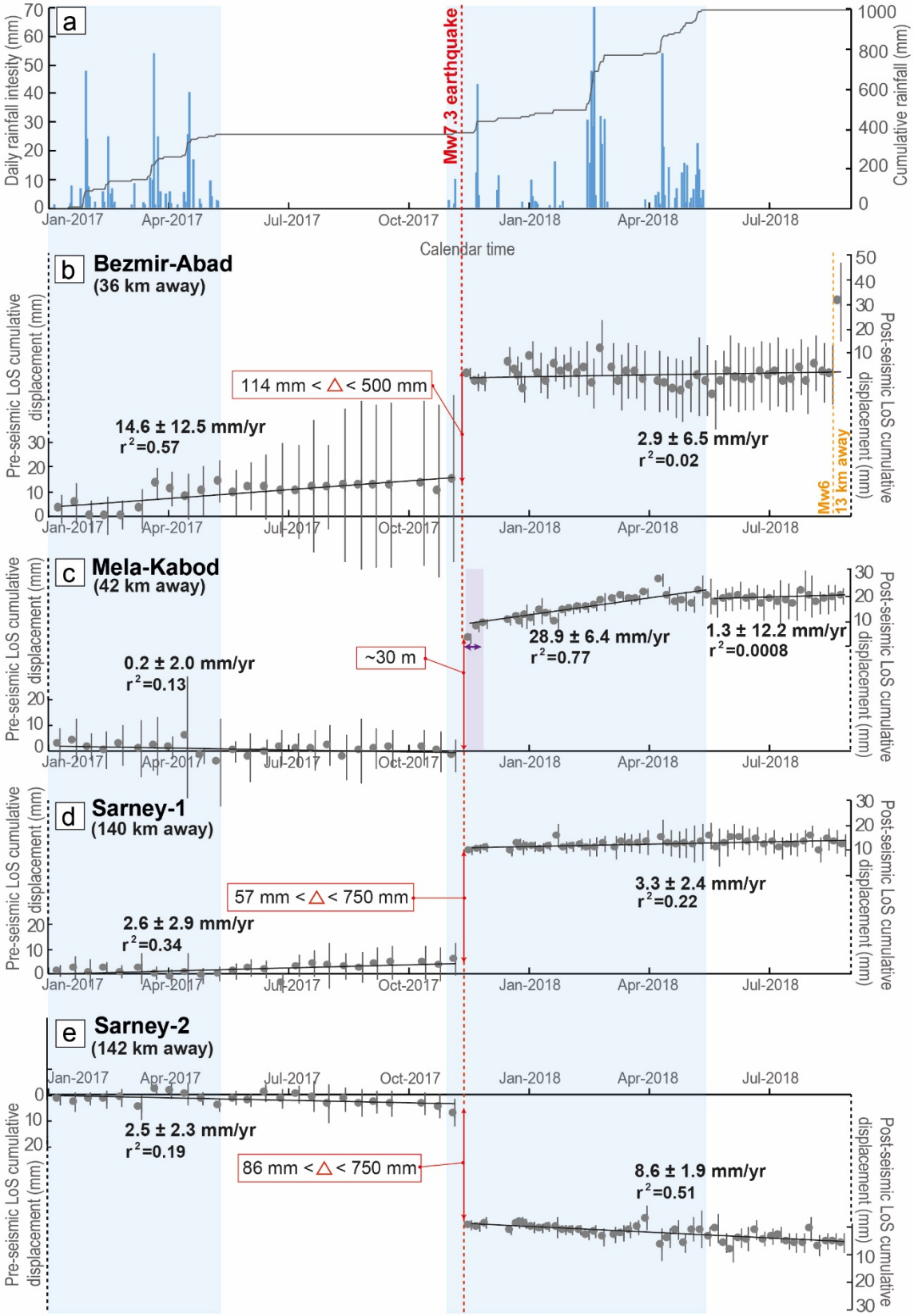
a
Daily rainfall intesity (mm)
Cumulative rainfall (mm)
Mw7.3 earthquake
Jan-2017
Apr-2017
Jul-2017
Oct-2017
Jan-2018
Apr-2018
Jul-2018
Calendar time
b
Bezmir-Abad
(36 km away)
Pre-seismic LoS cumulative displacement (mm)
Post-seismic LoS cumulative displacement (mm)
114 mm < △ < 500 mm
14.6 ± 12.5 mm/yr
r²=0.57
2.9 ± 6.5 mm/yr
r²=0.02
Mw6
13 km away
c
Mela-Kabod
(42 km away)
0.2 ± 2.0 mm/yr
r²=0.13
~30 m
28.9 ± 6.4 mm/yr
r²=0.77
1.3 ± 12.2 mm/yr
r²=0.0008
d
Sarney-1
(140 km away)
57 mm < △ < 750 mm
2.6 ± 2.9 mm/yr
r²=0.34
3.3 ± 2.4 mm/yr
r²=0.22
e
Sarney-2
(142 km away)
2.5 ± 2.3 mm/yr
r²=0.19
86 mm < △ < 750 mm
8.6 ± 1.9 mm/yr
r²=0.51

348

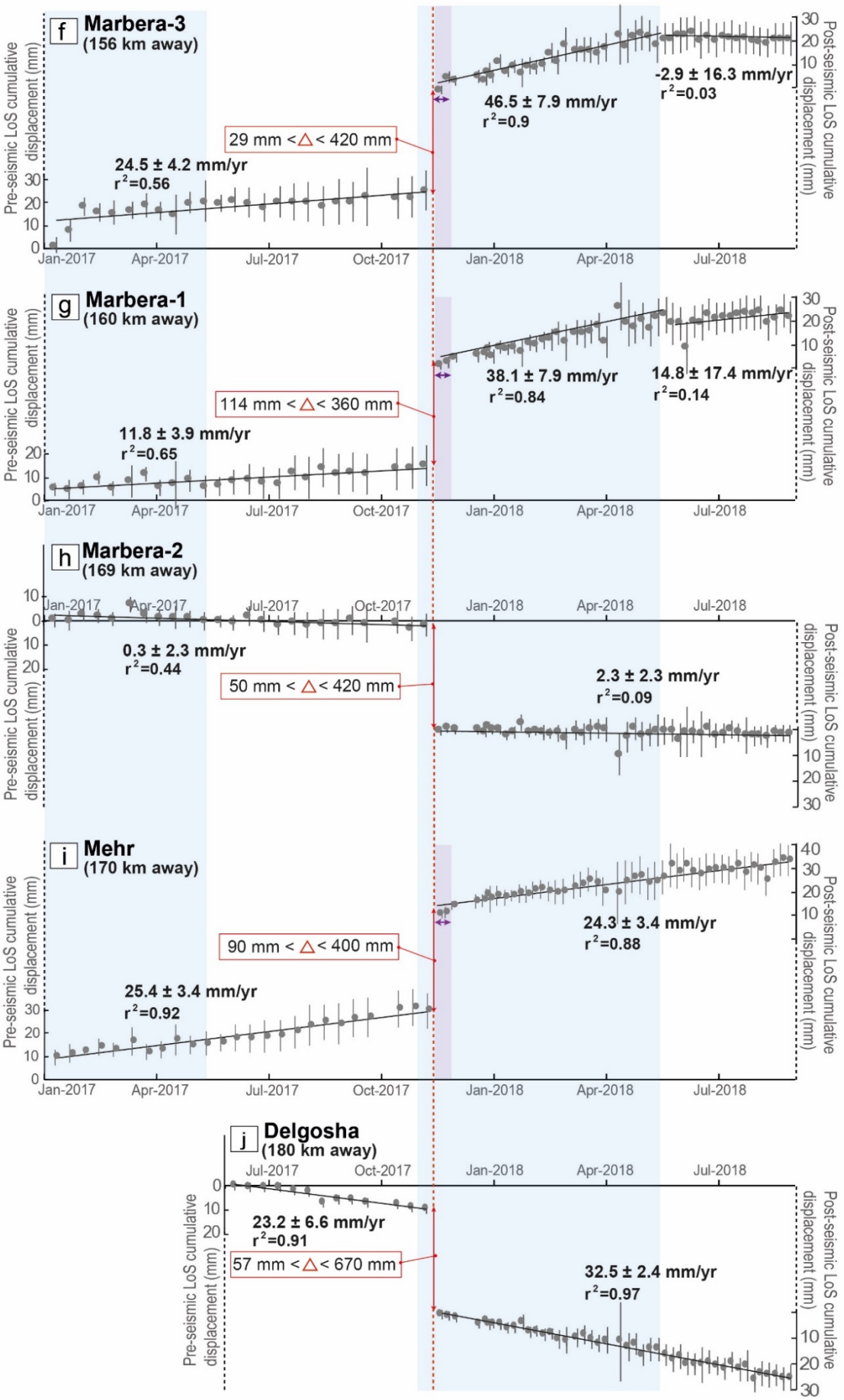
f Marbera-3
(156 km away)
29 mm < △ < 420 mm
24.5 ± 4.2 mm/yr
r²=0.56
46.5 ± 7.9 mm/yr
r²=0.9
-2.9 ± 16.3 mm/yr
r²=0.03
g Marbera-1
(160 km away)
114 mm < △ < 360 mm
11.8 ± 3.9 mm/yr
r²=0.65
38.1 ± 7.9 mm/yr
r²=0.84
14.8 ± 17.4 mm/yr
r²=0.14
h Marbera-2
(169 km away)
0.3 ± 2.3 mm/yr
r²=0.44
50 mm < △ < 420 mm
2.3 ± 2.3 mm/yr
r²=0.09
i Mehr
(170 km away)
90 mm < △ < 400 mm
25.4 ± 3.4 mm/yr
r²=0.92
24.3 ± 3.4 mm/yr
r²=0.88
j Delgosha
(180 km away)
23.2 ± 6.6 mm/yr
r²=0.91
57 mm < △ < 670 mm
32.5 ± 2.4 mm/yr
r²=0.97
Pre-seismic LoS cumulative displacement (mm)
Post-seismic LoS cumulative displacement (mm)
Jan-2017
Apr-2017
Jul-2017
Oct-2017
Jan-2018
Apr-2018
Jul-2018

Fig. 9 (a) Cumulative rainfall and rainfall intensity collected at the Ilam meteorological station (Fig. 1b; National Climatic Data Center). (b) to (j) Cumulative LOS displacement time-series with the error bars, computed for all the detected rockslides from InSAR over 20 months spanning the Mw 7.3 Sarpol-Zahab earthquake. The coseismic motion (Δ) is fixed for all time-series. The pre-seismic InSAR time-series for the Delgosha rockslide (j) extends back only 6 months before the earthquake due to unavailable data. The purple horizontal double arrow indicates the post-seismic relaxation period observed for some of the landslides.

5. Discussion

5.1. Uncertainty on the detection of landslides

The Sarpol-Zahab earthquake induced coseismic displacements for two types of landslides: 386 small disrupted slides clustered in a radius of a few tens of kilometers around the epicenter, and 9 giant rockslides, 7 of which are located in the far-field (up to 5 times the fault length). The validation of this inventory is complex due to the lack of accurate field observations, except for the well-detected Mela-Kabod giant landslide (Vajedian et al., 2018; Miyajima et al., 2018; Goorabi, 2020). The smallest disrupted slide detected has an area of 200 m² but smaller scale events certainly occurred, as suggested by field observations (Miyajima et al., 2018), which can therefore not be captured by our inventory. Also, the complex coseismic InSAR images makes the detection of landslide-like patterns difficult in the area affected by the strongest earthquake deformation (Fig. 7b). Thereof, there is a possibility that coherent landslides with small displacements (< 0.9 m) in this area were not identified. On the other hand, landslides with large coseismic displacement such as the Mela Kabod landslide cannot be detected by InSAR due to phase decoupling (Goorabi, 2020). Finally, small coherent landslides (area less than ~10^4 m²) with displacement less than one meter are not detected by our methodology due to the limited resolution of the Sentinel-1 SAR data (~4x15m original pixel size, 30x30m after multi-looking).

5.2 Controlling factors of disrupted landslides

Disrupted landslides are spread over ca. 140 km all along the fault plane with a higher concentration around the epicenter (Fig. 4), as commonly observed during earthquakes (e.g. Gorum et al., 2011; Gorum et al., 2014). The highest concentration is located northwest of the epicenter, and the farthest disrupted landslide was triggered 90 km south of the epicenter. The landslide concentration observed to the northwest is not consistent with the southward directivity of the source and the co-seismic slip displacement inferred from (Gombert et al. 2019), contrary to what was observed for other earthquakes (e.g. Gorum et al., 2011; Specht et al., 2019). Only few seismological stations were installed near the epicenter,

making it challenging to resolve the spatial distribution of the seismic ground motion in this area. Five seismic stations are available within 50 km of the epicenter (https://earthquake.usgs.gov/earthquakes/eventpage/us2000bmcg/shakemap/pga). In the area of high landslide concentration, 28 to 35 km north of the epicenter, three stations recorded PGA values between 0.27g and 0.57g, whereas the highest ground motion is recorded 40 km south of the epicenter in Sarpol-Zahab city (in an area with little topography and few landslides) with a peak ground acceleration of 0.76g. This strong asymmetry of the ground motion associated with the fault rupture directivity (Babaie Mahani and Kazemian, 2018; Gombert et al., 2019) is not reflected in the spatial distribution of landslides. Instead, the cluster of disrupted landslides northwest of the epicenter may be explained by the steep topography of the area (Fig. 4 and Fig. 5). Finally, although some small landslides may have been missed in our inventory (see discussion above), the number of recorded landslides (about 400) is still very low for a Mw7.3 earthquake, which would be expected to trigger a few thousand landslides in such a mountainous area (Keefer, 2002, Tanyas et al., 2017). This low number of landslides is, however, consistent with other observations from arid and semi-arid environments (Lacroix et al., 2013; Barlow et al., 2015). For this earthquake, we suggest that it can be explained by (1) the aridity of the region, which limits weathering and soil production (Singer, 1991; Dregne, 1976), and (2) relatively deep (and blind) thrust faulting, which induces lower ground motions than surface rupturing earthquakes (Aki, 1987).

5.3 Far field forcing of coherent landslides

The striking feature of this earthquake resides in the coseismic motion of the giant paleo-rockslides located at epicentral distances of up to 180 km (Fig. 7 and S1). For such a high magnitude earthquake (Mw 7.3), this distance corresponds to the upper bound, as can be inferred from worldwide data base of seismically induced landslides (Keefer, 2002; Delgado et al. 2011). The concentration and the huge size (volumes up to 2 km^3) of the rockslides triggered by this earthquake is however intriguing and, to our knowledge, has never been reported so far from the epicenter (4-5 times the fault length).

All these giant rockslides were pre-existing features with very large slide displacements accumulated in the past (a few hundred meters), and for most of them still active before the earthquake (Fig. 8, Table 2) highlighting their unstable character. All these rockslides are situated south of the epicenter in the direction of the rupture. As emphasized by several authors (Chen et al., 2018; Gombert et al., 2019) the directivity of the rupture toward the south led to stronger ground motion south compared to north of the rupture (Babaie Mahani and Kazemian, 2018). The recorded PGA closest to these rockslides reached 0.13g at the Ilam station (146 km far from the epicenter) and is significantly higher than the PGA recorded north of the epicenter at approximately the same distance (0.03g in Mahabad or Bukan stations).

The ground shaking can also be amplified by both local topographic and geologic effects (e.g. Murphy, 2015), more specifically as several rockslides developed on flanks of anticline ridges and in mechanically heterogeneous lithologies. Indeed, the five more distant giant landslides affected the same 200 m thick Ilam formation (limestone) overlying a 100 m thick shale layer (Surgah formation). This two-layer structure constitutes a dynamic oscillator on the thick underlying carbonate of the Sarvak formation, generating resonance and favoring rock sliding initiation along the weak shale layer. During the long-distance slide of the rockslides, the limestone blocks progressively disintegrated and dragged part of the Surgah formation, creating a highly destructive deposit with a maximum thickness (*t*) of around 150 m, consisting mainly of a mixture of shale and limestone. The amplification of the seismic waves during the earthquake is due to the seismic impedance contrast (product of the density ρ and shear wave velocity Vs) between this deposit and the underlying calcareous substratum. For vertically incident SH waves in a 1D elastic structure, the resonance frequency f_0 and the corresponding amplification Af_0 are given by (Kramer, 1996):

$$f_0 = \frac{Vs_D}{4t} \quad (1)$$

$$Af_0 = \frac{\rho_B Vs_B}{\rho_D Vs_D} \quad (2)$$

where Vs_D and Vs_B are the shear wave velocities of the rockslide deposit and the bedrock, respectively, and ρ_D and ρ_B are the corresponding densities.

Rockslide deposit and bedrock Vs values at these sites are not available, but plausible values can be taken from a similar rockslide comprising limestone and marls (e.g. Socco et al., 2010), and bedrock (e.g. Telford et al., 1990): Vs_D= 600 m/s; Vs_B= 3000 m/s; ρ_D= 2; ρ_B= 2.5. Considering these values, a resonance frequency $f_0 \approx 1$ Hz with a 1D amplification over 6 has been obtained. This resonance frequency, around 1Hz, is compatible with the frequency content of the earthquake source at such large distances (Babaie Mahani and Kazemian, 2018), suggesting a potential amplification effect that can thus favor landslide triggering.

Interestingly, several other ancient landslides previously mapped in this region (Ghazipour and Simpson, 2016) were not reactivated during the Sarpol-Zahab earthquake (Fig. 1b). Some explanations can be given for this phenomenon: (1) these landslides were inactive during the whole period of monitoring, thus indicating their higher stability; (2) they mostly occurred in different lithologies (Oligocene and Eocene units) with a structure (absence of shale layer) less sensitive to sliding and seismic amplification; (3) these non-reactivated landslides are mostly northwest oriented while the reactivated

ones are oriented northeast or southwest. Stronger seismic ground motions have been recorded perpendicular to the fault for long-period waves (Babaie Mahani and Kazemian, 2018), favoring the initiation of NE-SW oriented landslides.

5.4 Post-seismic motion of coherent landslides

The 9 giant rockslides present a co-seismic motion of at least 10 cm, 4 of them (Fig. 9c, f, g, i) being affected by a transient increase of the post-seismic velocity of a few mm in the 20 days following the earthquake. This co-seismic and relaxation process is consistent with previous observations (Lacroix et al., 2014), although the ratio between co- and post-seismic motion is far greater here, with most of the motion released during the co-seismic phase (against 3 to 10 times more post-seismic than co-seismic motion released on the Maca landslide, Peru - see Lacroix et al., 2014; Bontemps et al., 2020). Five of the landslides do not even present a post-seismic relaxation phase. These observations suggest that the rheology of the sliding surface does not follow strain-weakening friction laws (Lacroix et al., 2014), a rheology which can be caused by undrained loading of the landslide sliding surface during the shaking (Wang and Sassa, 2002) and progressive release of excess pore-water out of the loaded sliding surface.

Time-series of landslide kinematics also reveal an increase of the post-seismic annual velocity compared to the pre-seismic annual velocity for at least 5 of the studied rockslides (Fig. 9c, e, f, g, j). For 3 of the rockslides (Mela-Kabod, Marbera-1, Marbera-3) we document a higher velocity during the 2018 rainy season (Fig. 9c, f, g) followed by a subsequent decrease in velocity, eventually returning to the pre-earthquake velocity during the dry season. This observation may suggest a seasonal motion and threshold rainfall effects on the landslide kinematics (Zerathe et al., 2016). Furthermore, moderate earthquakes (Mw5-6) that occurred close to the landslides (Fig. 1b) may have contributed to the transient velocity increase by damaging rocks, thus promoting water infiltration (Bontemps et al., 2020) up to the impermeable formation (e.g. Surgah). However, exploring these issues are beyond the scope of this study, as this will require longer time-series and detailed field measurements of hydrologic and kinematic parameters (e.g. Schulz et al., 2009).

6. Conclusions

In this paper we provide an inventory of landslides induced by the Mw 7.3 Sarpol-Zahab earthquake which struck the northern Zagros Mountains on the 12th November 2017. To detect a maximum of triggered landslides of various sizes, typologies, and co-seismic displacements, we performed: (1) a visual change detection comparing orthorectified Planet

optical satellite images (3-4 m resolution) spanning the earthquake, (2) optical image correlations using SPOT6/7 (1.5 m resolution) and Planet images spanning the earthquake, and (3) InSAR detection and monitoring using Sentinel-1 images. With this strategy, 395 triggered landslides of different sizes and kinematics were detected, including 386 rockfalls concentrated within a radius of 40 km around the epicenter and 9 pre-existing giant rockslides (area range 3-30 km^2) distributed at distances between ~40 km and up to 180 km from the epicenter. Results revealed the exceptionally low number of landslides recorded during this Mw 7.3 earthquake, which is attributed to the semi-arid conditions of the Zagros Mountains that limit weathering and soil production. On the other hand, the striking element revealed by this earthquake-induced landslide inventory was the co-seismic displacement of 9 pre-existing giant rockslides, with minimum displacements ranging between 10 and 90 cm. Seven of these coherent landslides are clustered in the far field at distances of 140-180 km from the epicenter (4-5 times the fault length), and affect old deposits generated by the slide of a thick limestone layer over a shale formation on limbs of anticlinal structures striking NW-SE. We propose that the co-seismic forcing of these rockslides may be related to a combined effect of the southward directivity of the source, the NE-SW polarization of the ground motions, their sensitivity to low-frequencies (~1 Hz), the site effect due to the seismic impedance contrast on the flanks of the anticlines, and their pre-existing activity. From the InSAR time-series documenting the rockslide displacements (covering 20 months centered on the earthquake date), we observed that half of those giant rockslides were already slowly moving before the earthquake (velocity < 25 mm/yr).

Finally, most of these giant coherent rockslides have certainly been initiated several millennia ago, as shown by the dating of the giant Seymareh landslide (Roberts and Evans, 2013). The aridity of the area helped to preserve their geomorphology, and open the possibility to date the scarp evolution (e.g. LeRoux et al., 2009) for a long-term study of the landslide kinematics. The recent activity documented here shows the interest of these objects for landslide forcing studies over both short and long term of arid environments.

Acknowledgements

This research is funded by the Lebanese National Council for Scientific Research (CNRS). The authors also thank the support of the French Spatial Agency (CNES). SPOT images were acquired through the DINAMIS program. Supplementary figures are provided in the supporting information accompanying the main text. The data archiving is underway on the PerSCiDO platform.

References

Aki K (1987) Strong Motion Seismology BT - Strong Ground Motion Seismology. In: Erdik MÖ, Toksöz MN (eds). Springer Netherlands, Dordrecht, pp 3–39

Alavi, M (2007) Structures of the Zagros fold-thrust belt in Iran. American Journal of science, 307(9): 1064-1095.

Ambraseys NN, Melville CP (2005) A history of Persian earthquakes. Cambridge University Press, Cambridge [Cambridgeshire]; New York

Babaie Mahani A, Kazemian J (2018) Strong ground motion from the November 12, 2017, M 7.3 Kermanshah earthquake in western Iran. J Seismol 22:1339–1358. https://doi.org/10.1007/s10950-018-9761-x

Barlow J, Barisin I, Rosser N, et al (2015) Seismically-induced mass movements and volumetric fluxes resulting from the 2010 Mw=7.2 earthquake in the Sierra Cucapah, Mexico. Geomorphology 230:138–145. https://doi.org/10.1016/j.geomorph.2014.11.012

Barnhart WD, Brengman CMJ, Li S, Peterson KE (2018) Ramp-flat basement structures of the Zagros Mountains inferred from co-seismic slip and afterslip of the 2017 Mw7.3 Darbandikhan, Iran/Iraq earthquake. Earth Planet Sci Lett 496:96–107. https://doi.org/10.1016/j.epsl.2018.05.036

Beyer RA, Alexandrov O, McMichael S (2018) The Ames Stereo Pipeline: NASA's Open Source Software for Deriving and Processing Terrain Data. Earth Sp Sci 5:537–548. https://doi.org/10.1029/2018EA000409

Bontemps N, Lacroix P, Doin MP (2018) Inversion of deformation fields time-series from optical images, and application to the long term kinematics of slow-moving landslides in Peru. Remote Sens Environ 210:144–158. https://doi.org/10.1016/j.rse.2018.02.023

Bontemps N, Lacroix P, Larose E, et al (2020) Rain and small earthquakes maintain a slow-moving landslide in a persistent critical state. Nat Commun 11:780. https://doi.org/10.1038/s41467-020-14445-3

Bozzano F, Lenti L, Martino S, et al (2008) Self-excitation process due to local seismic amplification responsible for the reactivation of the Salcito landslide (Italy) on 31 October 2002. J Geophys Res Solid Earth 113:1–21. https://doi.org/10.1029/2007JB005309

Chen K, Xu W, Mai PM, et al (2018) The 2017 Mw 7.3 Sarpol Zahāb Earthquake, Iran: A compact blind shallow-dipping

513 thrust event in the mountain front fault basement. Tectonophysics 747–748:108–114.
514 https://doi.org/10.1016/j.tecto.2018.09.015

515 Delchiaro M, Della Seta M, Martino S, et al (2019) Reconstruction of river valley evolution before and after the
516 emplacement of the giant Seymareh rock avalanche (Zagros Mts., Iran). Earth Surf Dyn 7:929–947.
517 https://doi.org/10.5194/esurf-7-929-2019

518 Delgado J, Garrido J, López-Casado C, et al (2011) On far field occurrence of seismically induced landslides. Eng Geol
519 123:204–213. https://doi.org/10.1016/j.enggeo.2011.08.002

520 Dini B, Manconi A, Loew S (2019) Investigation of slope instabilities in NW Bhutan as derived from systematic DInSAR
521 analyses. Eng Geol 259:105111. https://doi.org/https://doi.org/10.1016/j.enggeo.2019.04.008

522 Doin M-P, Lodge F, Guillaso S, et al (2011) Presentation of the small baseline NSBAS processing chain on a case example:
523 the Etna deformation monitoring from 2003 to 2010 using Envisat data. Proc ESA 'Fringe 2011 Work Frascati, Italy,
524 (19-23 Sept 2011) 2011:19–23

525 Doin MP, Lasserre C, Peltzer G, et al (2009) Corrections of stratified tropospheric delays in SAR interferometry:
526 Validation with global atmospheric models. J Appl Geophys 69:35–50.
527 https://doi.org/https://doi.org/10.1016/j.jappgeo.2009.03.010

528 Dregne, HE (1976) Soils of arid regions. Amsterdam, Elsevier Scientific Pub. Co. http://site.ebrary.com/id/10276450.

529 Fan X, Scaringi G, Korup O, et al (2019) Earthquake-Induced Chains of Geologic Hazards: Patterns, Mechanisms, and
530 Impacts. Rev Geophys 57:421–503. https://doi.org/10.1029/2018RG000626

531 Ghazipour N, Simpson G (2016) Size distribution and controls of landslides in the Zagros mountain belt (Iran). Tecton
532 Evol Collision, Seism Southwest Asia<subtitle>In Honor Man Berberian's Forty-Five Years Res Contrib 525:.
533 https://doi.org/10.1130/2016.2525(13)

534 Gombert B, Duputel Z, Shabani E, et al (2019) Impulsive Source of the 2017 MW=7.3 Ezgeleh, Iran, Earthquake.
535 Geophys Res Lett 46:5207–5216. https://doi.org/10.1029/2018GL081794

536 Goorabi A (2020) Detection of landslide induced by large earthquake using InSAR coherence techniques – Northwest
537 Zagros, Iran. Egypt J Remote Sens Sp Sci 23:195–205. https://doi.org/10.1016/j.ejrs.2019.04.002

538 Gorum T, Fan X, van Westen CJ, et al (2011) Distribution pattern of earthquake-induced landslides triggered by the 12
539 May 2008 Wenchuan earthquake. Geomorphology 133:152–167.

https://doi.org/https://doi.org/10.1016/j.geomorph.2010.12.030

Gorum T, Korup O, van Westen CJ, et al (2014) Why so few? Landslides triggered by the 2002 Denali earthquake, Alaska. Quat Sci Rev 95:80–94. https://doi.org/https://doi.org/10.1016/j.quascirev.2014.04.032

Guzzetti F, Mondini AC, Cardinali M, et al (2012) Landslide inventory maps: New tools for an old problem. Earth-Science Rev 112:42–66. https://doi.org/https://doi.org/10.1016/j.earscirev.2012.02.001

Harp EL, Hartzell SH, Jibson RW, et al (2014) Relation of Landslides Triggered by the Kiholo Bay Earthquake to Modeled Ground Motion. Bull Seismol Soc Am 104:2529–2540. https://doi.org/10.1785/0120140047

Harp, EL, Jibson, RW (1995) Inventory of landslides triggered by the 1994 Northridge, California earthquake: U.S. Geological Survey Open-File Report 17:95-213.

Harp EL, Wilson RC (1995) Shaking intensity thresholds for rock falls and slides: Evidence from 1987 Whittier Narrows and superstition hills earthquake strong-motion records. Bull Seismol Soc Am 85:1739–1757

Hessami K, Jamali F, Tabassi H (2003) Map of major active faults of Iran (scale 1: 2,500,000).

Homke S, Vergés J, Serra-Kiel J, et al (2009) Late Cretaceous–Paleocene formation of the proto–Zagros foreland basin, Lurestan Province, SW Iran. Geological Society of America Bulletin, 121(7-8), 963-978.

Huber, H (1976) Tectonic map of south-west of Iran, 1:2500000. National Iranian Oil Company, Exploration and Production.

Keefer DK (2002) Investigating landslides caused by earthquakes - A historical review. Surv Geophys 23:473–510. https://doi.org/10.1023/A:1021274710840

Keefer DK (1984) Geological Society of America Bulletin Landslides caused by earthquakes. https://doi.org/10.1130/0016-7606(1984)95<406

Kramer SL (1996) GEOTECHNICAL EARTHQUAKE ENGINEERING Kramer 1996.pdf. 376

Lacroix P (2016) Landslides triggered by the Gorkha earthquake in the Langtang valley, volumes and initiation processes. Earth, Planets Sp 68:46. https://doi.org/10.1186/s40623-016-0423-3

Lacroix P, Bièvre G, Pathier E, et al (2018) Use of Sentinel-2 images for the detection of precursory motions before landslide failures. Remote Sens Environ 215:507–516. https://doi.org/10.1016/j.rse.2018.03.042

Lacroix P, Perfettini H, Taipe E, Guillier B (2014) Coseismic and postseismic motion of a landslide: Observations,

566 modeling, and analogy with tectonic faults. Geophys Res Lett 41:6676–6680.
567 https://doi.org/10.1002/2014GL061170

568 Lacroix P, Zavala B, Berthier E, Audin L (2013) Supervised method of landslide inventory using panchromatic SPOT5
569 images and application to the earthquake-triggered landslides of Pisco (Peru, 2007, Mw8.0). Remote Sens 5:2590–
570 2616. https://doi.org/10.3390/rs5062590

571 Le Roux O, Schwartz S, Gamond JF, et al (2009) CRE dating on the head scarp of a major landslide (Séchilienne, French
572 Alps), age constraints on Holocene kinematics. Earth Planet Sci Lett 280:236–245.
573 https://doi.org/https://doi.org/10.1016/j.epsl.2009.01.034

574 Leprince S, Barbot S, Ayoub F, Avouac JP (2007) Automatic and precise orthorectification, coregistration, and subpixel
575 correlation of satellite images, application to ground deformation measurements. IEEE Trans Geosci Remote Sens
576 45:1529–1558. https://doi.org/10.1109/TGRS.2006.888937

577 Llewellyn, PG (1974) Geological compilation map, Ilam-Kuhdasht (Map NO.20504). Tehran:Oil Service Company of
578 Iran.

579 Marano KD, Wald DJ, Allen TI (2010) Global earthquake casualties due to secondary effects: a quantitative analysis for
580 improving rapid loss analyses. Nat Hazards 52:319–328. https://doi.org/10.1007/s11069-009-9372-5

581 Marc, O., Hovius, N., Meunier, P., Gorum, T., & Uchida, T. (2016). A seismologically consistent expression for the total
582 area and volume of earthquake-triggered landsliding. J Geophys Res: ES, 121:640-663.

583 Marc O, Hovius N, Meunier P, et al (2015) Transient changes of landslide rates after earthquakes. Geology 43:883–886.
584 https://doi.org/10.1130/G36961.1

585 Masson F, Lehujeur M, Ziegler Y, Doubre C (2014) Strain rate tensor in Iran from a new GPS velocity field. Geophys J
586 Int 197:10–21. https://doi.org/10.1093/gji/ggt509

587 McQuarrie N, Stock JM, Verdel C, Wernicke BP (2003) Cenozoic evolution of Neotethys and implications for the causes
588 of plate motions. Geophys Res Lett 30:30–33. https://doi.org/10.1029/2003GL017992

589 Meunier P, Hovius N, Haines AJ (2007) Regional patterns of earthquake-triggered landslides and their relation to ground
590 motion. Geophys Res Lett 34:1–5. https://doi.org/10.1029/2007GL031337

591 Meunier P, Hovius N, Haines JA (2008) Topographic site effects and the location of earthquake induced landslides. Earth
592 Planet Sci Lett 275:221–232. https://doi.org/https://doi.org/10.1016/j.epsl.2008.07.020

593 Miyajima M, Fallahi A, Ikemoto T, et al (2018) Site Investigation of the Sarpole-Zahab Earthquake, Mw 7.3 in SW Iran
594 of November 12, 2017. JSCE J Disaster FactSheets

595 Murphy B (2015) Chapter 4 - Coseismic Landslides. In: Shroder JF, Davies Risks and Disasters TBT-LH (eds).
596 Academic Press, Boston, pp 91–129

597 Nissen E, Ghods A, Karasözen E, et al (2019) The 12 November 2017 M w 7.3 Ezgeleh-Sarpolzahab (Iran) Earthquake
598 and Active Tectonics of the Lurestan Arc. J Geophys Res Solid Earth 124:2124–2152.
599 https://doi.org/10.1029/2018JB016221

600 Roback K, Clark MK, West AJ, et al (2018) The size, distribution, and mobility of landslides caused by the 2015 Mw7.8
601 Gorkha earthquake, Nepal. Geomorphology 301:121–138.
602 https://doi.org/https://doi.org/10.1016/j.geomorph.2017.01.030

603 Roberts NJ, Evans SG (2013) The gigantic Seymareh (Saidmarreh) rock avalanche, Zagros Fold-Thrust Belt, Iran. J Geol
604 Soc London 170:685–700. https://doi.org/10.1144/jgs2012-090

605 Rodríguez CE, Bommer JJ, Chandler RJ (1999) Earthquake-induced landslides: 1980–1997. Soil Dyn Earthq Eng
606 18:325–346. https://doi.org/https://doi.org/10.1016/S0267-7261(99)00012-3

607 Rosen PA, Hensley S, Peltzer G, Simons M (2004) Updated repeat orbit interferometry package released. Eos
608 (Washington DC) 85:47. https://doi.org/10.1029/2004EO050004

609 Saura E, Vergés J, Homke S, et al (2011). Basin architecture and growth folding of the NW Zagros early foreland basin
610 during the Late Cretaceous and early Tertiary. Journal of the Geological Society, 168:235-250.

611 Schulz WH, McKenna JP, Kibler JD, et al (2009) Relations between hydrology and velocity of a continuously moving
612 landslide-evidence of pore-pressure feedback regulating landslide motion?. Landslides 6:181–190.

613 Singer M J (1991) Physical properties of arid region soils. Semiarid lands and deserts: soils resource and reclamation, 81-
614 109.

615 Socco LV, Jongmans D, Boiero D, et al (2010) Geophysical investigation of the Sandalp rock avalanche deposits. J Appl
616 Geophys 70:277–291. https://doi.org/https://doi.org/10.1016/j.jappgeo.2009.12.005

617 Specht SV, Ozturk U, Veh G, et al (2019) Effects of finite source rupture on landslide triggering: The 2016 Mw 7.1
618 Kumamoto earthquake. Solid Earth 10:463–486. https://doi.org/10.5194/se-10-463-2019

619 Talebian M, Jackson J (2004) A reappraisal of earthquake focal mechanisms and active shortening in the Zagros mountains
620 of Iran. Geophys J Int 156:506–526. https://doi.org/10.1111/j.1365-246X.2004.02092.x

621 Tanyas H, van Westen CJ, Persello C, et al (2019) Rapid prediction of the magnitude scale of landslide events triggered
622 by an earthquake. Landslides, 16(4):661-676.

623 Tanyas H, van Westen CJ, Allstadt KE, et al (2017) Presentation and Analysis of a Worldwide Database of Earthquake-
624 Induced Landslide Inventories. J Geophys Res Earth Surf 122:1991–2015. https://doi.org/10.1002/2017JF004236

625 Tatard L, Grasso JR, Helmstetter A, Garambois S (2010) Characterization and comparison of landslide triggering in
626 different tectonic and climatic settings. J Geophys Res Earth Surf 115:1–18. https://doi.org/10.1029/2009JF001624

627 Telford WM, Geldart LP, Sheriff RE, Sheriff RE (1990) Applied geophysics. London:Cambridge university press.
628 doi:10.1017/CBO9781139167932.

629 Vajedian S, Motagh M, Mousavi Z, et al (2018) Coseismic deformation field of the Mw 7.3 12 November 2017 Sarpol-e
630 Zahab (Iran) earthquake: A decoupling horizon in the Northern Zagros Mountains inferred from InSAR
631 observations. Remote Sens 10:. https://doi.org/10.3390/rs10101589

632 Valagussa A, Marc O, Frattini P, Crosta GB (2019) Seismic and geological controls on earthquake-induced landslide size.
633 Earth Planet Sci Lett 506:268–281. https://doi.org/https://doi.org/10.1016/j.epsl.2018.11.005

634 Valkaniotis S, Foumelis M, Survey FG, et al (2018) Three - dimensional displacement field of a large co - seismic
635 landslide (2017 Iraq - Iran earthquake) using optical - image correlation and SAR pixel offset - tracking INQUA
636 Focus Group Earthquake Geology and Seismic Hazards

637 Wang G, Sassa K (2002) Post-failure mobility of saturated sands in undrained load-controlled ring shear tests. Can
638 Geotech J 39:821–837. https://doi.org/10.1139/t02-032

639 Wang W-N, Nakamura H, Tsuchiya S, Chen C-C (2002) Distributions of landslides triggered by the Chi-chi Earthquake
640 in Central Taiwan on September 21, 1999. Landslides 38:318–326. https://doi.org/10.3313/jls1964.38.4_318

641 Watkinson IM, Hall R (2019) Impact of communal irrigation on the 2018 Palu earthquake-triggered landslides. Nat Geosci
642 12:940–945. https://doi.org/10.1038/s41561-019-0448-x

643 Zerathe S, Lacroix P, Jongmans D, et al (2016) Morphology, structure and kinematics of a rainfall controlled slow-moving
644 Andean landslide, Peru. Earth Surf Process Landforms 41:1477–1493. https://doi.org/10.1002/esp.3913